RSC Advances

PAPER

View Article Online
View Journal | View Issue



Cite this: *RSC Adv.*, 2023, **13**, 17947

# An ionic liquid- and PEO-based ternary polymer electrolyte for lithium metal batteries: an advanced processing solvent-free approach for solid electrolyte processing†

Lukas Herbers, [a] Verena Küpers, [a] Martin Winter[ab] and Peter Bieker *[b]

A processing solvent-free manufacturing process for cross-linked ternary solid polymer electrolytes (TSPEs) is presented. Ternary electrolytes (PEODA, $Pyr_{14}TFSI$, LiTFSI) with high ionic conductivities of >1 mS $cm^{-1}$ are obtained. It is shown that an increased LiTFSI content in the formulation (10 wt% to 30 wt%) decreases the risk of short-circuits by HSAL significantly. The practical areal capacity increases by more than a factor of 20 from 0.42 mA h $cm^{-2}$ to 8.80 mA h $cm^{-2}$ before a short-circuit occurs. With increasing $Pyr_{14}TFSI$ content, the temperature dependency of the ionic conductivity changes from Vogel–Fulcher–Tammann to Arrhenius behavior, leading to activation energies for the ion conduction of 0.23 eV. In addition, high Coulombic efficiencies of 93% in Cu||Li cells and limiting current densities of 0.46 mA $cm^{-2}$ in Li||Li cells were obtained. Due to a temperature stability of >300 °C the electrolyte guarantees high safety in a broad window of conditions. In LFP||Li cells, a high discharge capacity of 150 mA h $g^{-1}$ after 100 cycles at 60 °C was achieved.

Received 14th April 2023
Accepted 30th May 2023

DOI: 10.1039/d3ra02488a

rsc.li/rsc-advances



## Introduction

Lithium (Li) metal has become the focus of extensive research in the past years.[1] Its high gravimetric capacity of 3860 mA h $g^{-1}$ and low standard reduction potential of −3.04 V *vs.* standard hydrogen electrode (SHE) make it an ideal choice for a negative electrode active material in high energy density batteries.[2] Nonetheless, the application of Li metal has major challenges.[3] The decomposition of the electrolyte, the formation of the Solid Electrolyte Interphase (SEI) and the accumulation of inhomogeneous Li metal deposits, respectively 'high surface area lithium (HSAL)' and 'dead Li' cannot only result in active lithium loss (ALL) but also safety concerns.[4–6] In particular, the risk of short-circuits by HSAL and the high reactivity of liquid flammable electrolytes with HSAL can be hazardous.[7,8] To overcome these safety concerns, solid electrolytes (SE) and electrolytes based on ionic liquids are considered as safer alternatives.[9–11]

Solid electrolytes are often divided into the categories of inorganic solid electrolytes (ISEs), solid polymer electrolytes (SPEs) and composite polymer-inorganic electrolytes (CPIEs).[12] The most studied polymer for Li-based batteries is poly ethylene oxide (PEO) due to its ether-functional groups combined with an alkyl-segment.[13] The ether groups interact with Li-ions, granting a great Li salt solubility as well as good ion transport properties.[13] Despite the benefit in safety of PEO electrolytes, they usually suffer from a low room temperature (RT) ionic conductivity.[14] In comparison, several ISEs provide sufficient ionic conductivity. Nonetheless, ISEs can have challenges on their own, for instance a narrow electrochemical stability window, an expensive synthesis or poor electrode|electrolyte compatibility due to a low mechanical flexibility.[15,16] Therefore, hybrids of different types of electrolytes are useful to balance the requirements of processability, ionic conductivity, safety and reversibility of Li metal electrodeposition and -dissolution.[17,18] ISEs, SPEs and/or liquid electrolytes can therefore be combined to form CPIEs, gel and pseudo-solid electrolytes. The combination of polymers with RT ionic liquids (IL) and Li salts results in so called ternary solid polymer electrolytes (TSPE), with significantly higher ionic conductivities compared to SPEs and greater mechanical flexibility than ISEs.[19,20] Moreover, while more expensive than organic solvent-based electrolytes, the low vapor pressure and high thermal stability of ionic liquids increases the safety compared to liquid organic electrolytes.[21]

Nonetheless, despite the higher performance by improved ionic conductivity compared to SPEs, TSPEs also show major challenges which need to be addressed to make them applicable in Li metal full cells. As shown by Zhang *et al.* a PEO-based TSPE ($PEO_{ref}$) with a molar ratio of 10 : 1 : 2 (EO : LiTFSI (lithium bis(trifluoromethanesulfonyl)imide) : $Pyr_{14}TFSI$ (1-butyl-1-

[a]*MEET Battery Research Center, Institute of Physical Chemistry, University of Münster, 48149 Münster, Germany*

[b]*Helmholtz-Institute Münster (HIMS), IEK-12, Forschungszentrum Jülich GmbH, 48149 Münster, Germany. E-mail: peter.bieker@uni-muenster.de*

† Electronic supplementary information (ESI) available. See DOI: https://doi.org/10.1039/d3ra02488a

methyl-pyrrolidinium bis(trifluoromethylsulfonyl)imide)) suffers from low mechanical stability (elastic modulus: 0.3 MPa at 20 °C).[20,22] This low mechanical strength results in a limited suppression of Li metal HSAL, which penetrates through the electrolyte leading to a cell short-circuit. In this work the ratio of polymer, Li salt and IL is balanced to benefit from the high ionic conductivity provided by the IL but at the same time enable short-circuit prevention by the high mechanical strength of Li salt and polymer. Furthermore, different from commonly used electrolyte processing by use of processing solvent-based casting or hot pressing of solids, which is expensive, time-consuming and in some cases even hazardous, in this work, only liquid or soluble precursors without any processing solvents are used. For this purpose, long chain solid PEO is replaced by PEODA (polyethylene oxide diacrylate), a small chain and therefore liquid SPE. Thus, the energy-consuming removal of the solvents during processing of solid CPIEs and TSPEs after solvent casting is not necessary. Also, in contrast to hot pressing, no elevated temperatures are needed, because the electrolyte can be processed under RT, making the presented electrolyte processing more time- and energy-efficient. During processing, the acrylate end groups of the PEODA are cross-linked by ultraviolet (UV) light induced radical cross-linking process, which leads to a fast phase transition from liquid to solid, enabling the combination of the processability of a liquid with the safety of a solid electrolyte. The ternary electrolyte composition is optimized towards a high conductivity and to meet the safety concerns regarding inhomogeneous Li electro-deposition and -dissolution, temperature stability and high voltage stability. Finally, the Li metal electrodeposition/-dissolution behavior in Li‖Li, Cu‖Li and lithium iron phosphate (LFP)‖Li cells and the electrochemical performance and limitations of the electrolyte in symmetric Li‖Li cells are determined.

# Experimental

## Chemicals

PEODA (Sigma-Aldrich, purity ≤100%, $M_n$ = 700) was stored over activated molecular sieve 3 Å for at least seven days before use (water content: 20 ± 3 ppm by Karl-Fischer titration). Benzophenone (BP) (Merck, purity = 99%) was used as received. $Pyr_{14}TFSI$ (Solvionic, purity = 99.9%) was dried for 48 hours at 110 °C under vacuum followed by 48 hours at 110 °C under high-vacuum $<10^{-7}$ mbar. LiTFSI (TCI, purity > 98%) was dried for at least 48 hours at 110 °C under vacuum followed by 48 hours at 110 °C under high-vacuum $<10^{-7}$ mbar. LFP sheets ($LiFePO_4$, NANOMYTE® BE-60E, experimental capacity ≥170 mA h $g^{-1}$, NEI Corporation) were dried for 48 hours at 100 °C under vacuum.

## Preparation of electrolyte films

Electrolyte films were prepared in a dry room. The electrolyte "$P_xIL_yS_z$" was named according to its mass ratios of $x$ PEODA "$P_x$", $y$ of the $Pyr_{14}TFSI$ "$IL_y$" and $z$ of LiTFSI "$S_z$", see Table 1. Different $x$, $y$, $z$ mass ratios were mixed with BP (1 wt% of the polymer content). Afterwards, the liquid mixture was filled into a polytetrafluoroethylene (PTFE) mold with two different mold heights of 250 ± 25 μm or 500 ± 50 μm and covered by a siliconized biaxial-oriented polyethylene terephthalate (boPET) foil. The electrolyte was placed in an UVACUBE 100 with a 100 W lamp (Dr Höhnle AG) and was irradiated by UV light for 10 min. The final electrolyte thicknesses were validated by a layer thickness gauge (Mitutoyo ABSOLUTE) after cross-linking. $PEO_{ref}$ was prepared as described elsewhere.[20,22]

Table 1 Abbreviation for $P_xIL_yS_z$

| Abbreviation | Component | Chemical |
|---|---|---|
| P | Polymer | PEODA |
| IL | Ionic liquid | $Pyr_{14}TFSI$ |
| S | Salt | LiTFSI |

The 851 Titrando Karl Fischer Coulometer (Metrohm, Herisau, Switzerland) was calibrated with a threefold measurement of a 100 mg $L^{-1}$ water standard for quantification. Each electrolyte was measured three times with an injection of 1 g. Instrument control, data acquisition and data evaluation were performed using tiamo™ 2.4 (Metrohm).[23]

The temperature stabilities of the electrolytes were studied using thermogravimetric analysis (TGA, A Q5000IR by TA instruments) with a heat rate of 10 K $min^{-1}$ from 20 °C to 600 °C.

Fourier-transform infrared spectroscopy (FT-IR) measurements were performed on a BRUKER ALPHA II. The samples were placed onto the attenuated total reflection (ATR) crystal and a wavenumber range from 4000 $cm^{-1}$ to 400 $cm^{-1}$ was measured.

For electrochemical measurements round electrolyte discs of 15 mm diameter and 250 μm thickness were assembled in Li‖Li, Cu‖Li, stainless steel (SST)‖Li, LFP‖Li and SST‖SST CR2032 two-electrode coin cells in a dry room. Temperature dependent ionic conductivity profiles were measured by impedance spectroscopy in SST‖SST cells on a Novocontrol Alpha Analyzer. An amplitude of 10 mV, a frequency range from 0.1 Hz to 10 MHz and a temperature interval from 0 °C to 80 °C in 10 °C steps were applied. Galvanostatic polarization tests (0.1 mA $cm^{-2}$, 0.5 mA h $cm^{-2}$, 50 cycles) with Li‖Li cells, galvanostatic discharge tests ('short-circuit tests', 0.1 mA $cm^{-2}$) with Li‖Li cells, galvanostatic polarization tests (0.05 mA $cm^{-2}$, 100 cycles, 2.5 V to 4.0 V) with LFP‖Li cells and galvanostatic polarization tests (0.1 mA $cm^{-2}$, 0.1 mA h $cm^{-2}$, 200 cycles, cutoff voltage ± 1 V) with Cu‖Li cells were performed on a MACCOR battery cycler (MACCOR Series 4000) at 60 °C. Linear sweep voltammetry tests (0.5 mV $s^{-1}$, from OCV (open-circuit voltage) to 6 V) in SST‖Li cells, charge pulse analysis tests (1.2 mA $cm^{-2}$, 1.4 mA $cm^{-2}$, 1.6 mA $cm^{-2}$, 1.8 mA $cm^{-2}$, 2.0 mA $cm^{-2}$ and 2.2 mA $cm^{-2}$, cutoff voltage 1 V, rest time between charge pulses 3 h) in Li‖Li cells and transference number measurements (10 mHz to 1 MHz, ± 10 mV, 20 ± 1 mV) in Li‖Li cells were performed on a VMP potentiostat (Bio-152 Logic) at 60 °C. A triple measurement set was performed for each technique.

## Results and discussion

### Processability

The processing of electrolytes of different composition is schematically given in Fig. 1. The mixture of precursors PEODA, $Pyr_{14}TFSI$ and LiTFSI results in a homogeneous liquid phase. PEODA is the key component enabling the fully liquid precursor as well as the solid final state of the electrolyte. Due to its small chain length, it is liquid at RT, making it a solvent-like component for LiTFSI. The ethylene oxide groups strongly interact with $Li^+$ ions and dissolve LiTFSI even at high weight ratios of 40% in contrast to pure $Pyr_{14}TFSI$-LiTFSI mixtures, which solidify at high LiTFSI contents. While the inner molecular chains $(-CH_2-CH_2-O-)_x$ are beneficial for the liquid state, the end groups ($CH_2$═CH–CO–O–R) of PEODA can lead to a phase formation of the electrolyte from liquid to solid. The acrylate groups at the end of the polymer chains contain double bonds that are cross-linked by radical induced polymerization.[24] The full cross-linking mechanism is given in Fig. 11 in the ESI.†

The cross-linking process is verified by FT-IR analysis. As shown in Fig. 2a, the non-cross-linked PEODA (blue curve) has a band in the absorption spectra at a wavenumber of 1636 $cm^{-1}$, which is caused by the valence vibration of the carbon–carbon double bond ($\nu$(C═C)). With increasing progress of the radical chain reaction, the peaks representing double bonds decrease, allowing to monitor the determination of the cross-linking

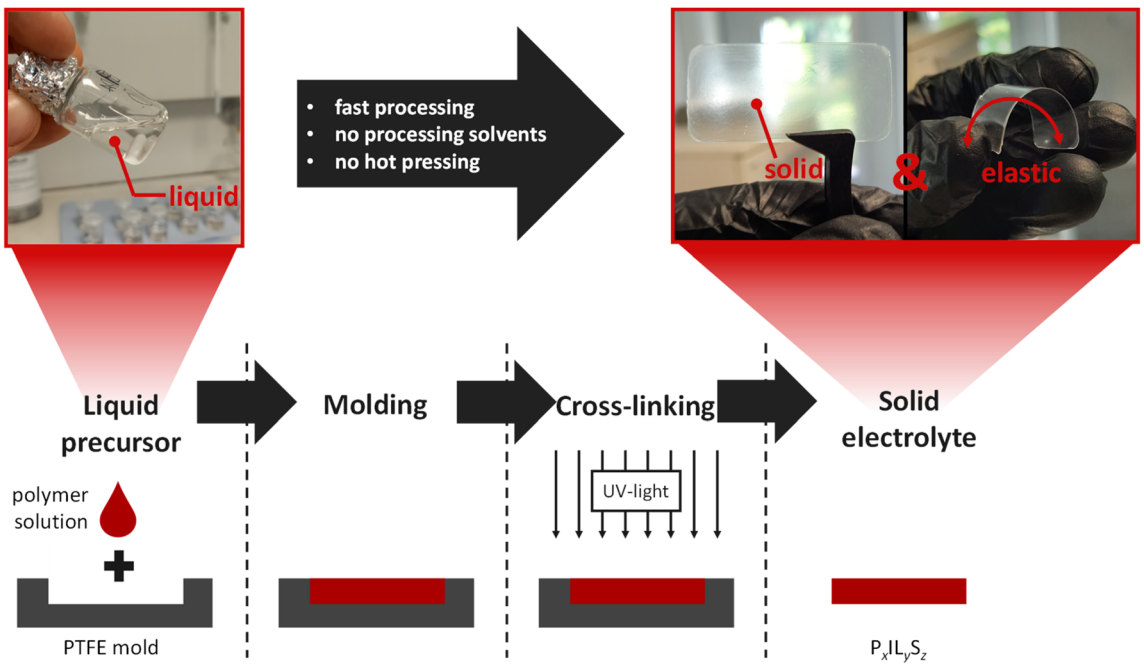


Fig. 1 Processing solvent-free preparation ternary electrolyte manufacturing (liquid precursor, molding, cross-linking, solid electrolyte).

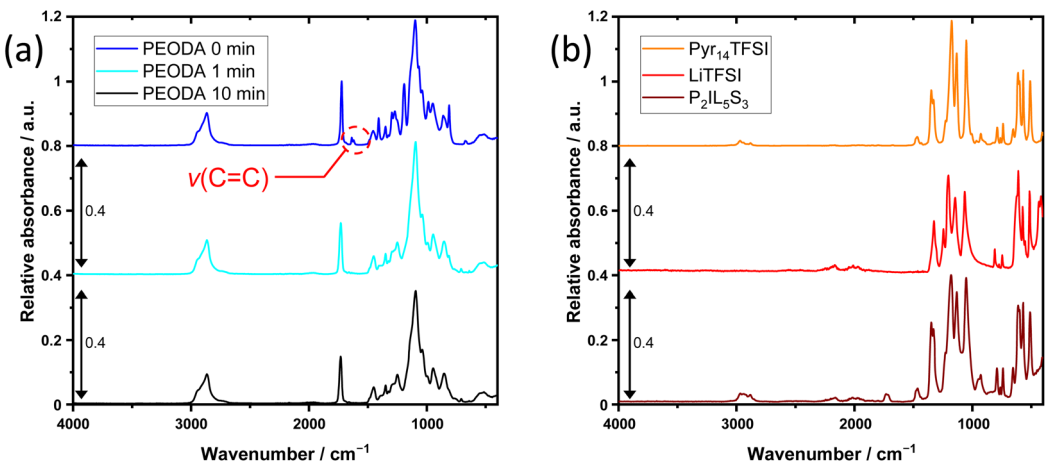


Fig. 2 Absorbance spectra of (a) $Pyr_{14}TFSI$, LiTFSI and $P_2IL_5S_3$ cross-linked for 10 min and (b) PEODA with 1 wt% of BP not cross-linked, cross-linked for 1 min and cross-linked for 10 min.

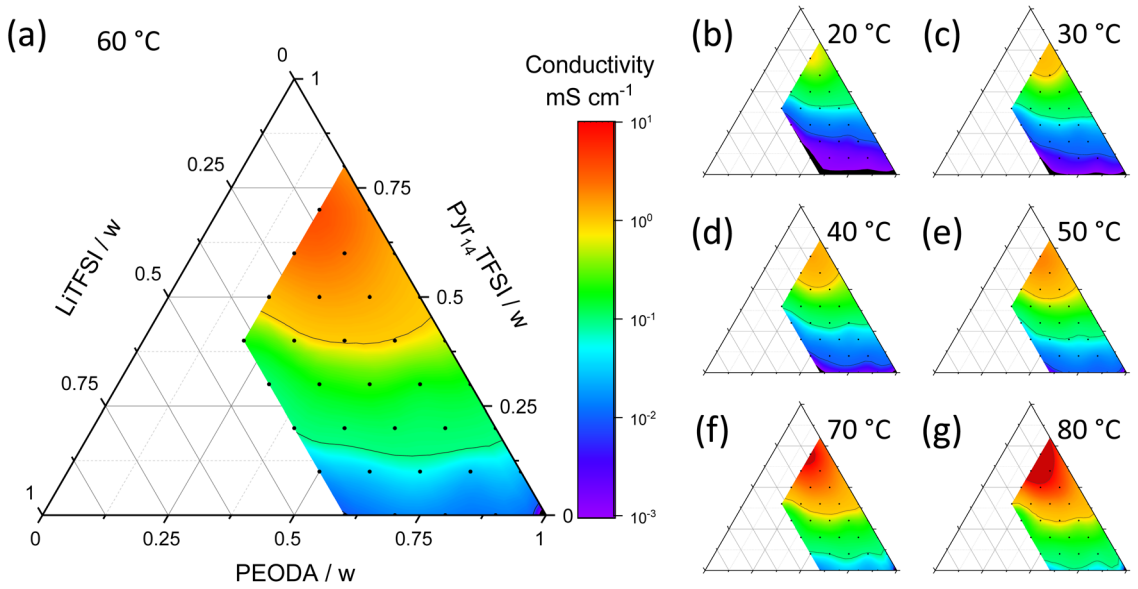


Fig. 3 Ionic conductivities of different electrolyte compositions at various temperatures. Ternary ionic conductivity diagram at (a) 60 °C; (b) 20 °C; (c) 30 °C; (d) 40 °C; (e) 50 °C; (f) 70 °C; (g) 80 °C. Black dots indicate a measured sample, ionic conductivities <$10^{-3}$ mS cm$^{-1}$ are marked in black and ionic conductivities of >10 mS cm$^{-1}$ are dark red regions.

process. As is seen from Fig. 2a no $\nu$(C=C) peak is observed even after 1 min of irradiation (cyan curve), indicating that despite the low weight percentage of photo initiator, the cross-linking is completed after 1 min, compare Fig. 12 in the ESI.† After 10 min of exposure to UV radiation (black curve) no further changes in the IR spectra are observed. To guarantee a fully cross-linked state even at lower polymer content, all electrolytes were cross-linked for an excessive time of 10 min. A spectra of the electrolyte $P_2IL_5S_3$ (brown curve) after 10 min of UV radiation, as well as the spectra of the pure $Pyr_{14}TFSI$ (orange curve) and pure LiTFSI (red curve) used for electrolyte mixing, are shown in Fig. 2b. No $\nu$(C=C) peak is observed in the $P_2IL_5S_3$ spectra. The resulting films are transparent, homogeneous, non-porous and elastic (elastic modulus: 3.2 MPa). (see Fig. 1 and 13 in the ESI†).

## Ionic conductivity

The ternary diagrams of various mass ratios of $Pyr_{14}TFSI$, LiTFSI and PEODA at different temperatures are shown in Fig. 3. The ionic conductivities from $10^{-3}$ mS cm$^{-1}$ (purple) to $10^{1}$ mS cm$^{-1}$ (red) are plotted over the composition in weight fraction. Seven temperatures from 20 °C to 80 °C are shown. Due to viscosity limitations the weight fraction of LiTFSI is restricted to a maximum of 0.4. The polymer content is kept between 0.2 and 1.0 to enable sufficient mechanical stability of the electrolyte.

An ionic conductivity of ≥1 mS cm$^{-1}$ is considered as a benchmark in literature.[17,25] This benchmark is not reached for a temperature of 20 °C independent of the mass ratios of the ternary electrolyte, see Fig. 3b, but at slightly elevated temperature of 30 °C (Fig. 3c) for high $Pyr_{14}TFSI$ fractions. An ionic conductivity of ≥1 mS cm$^{-1}$ is achieved for smaller fractions of

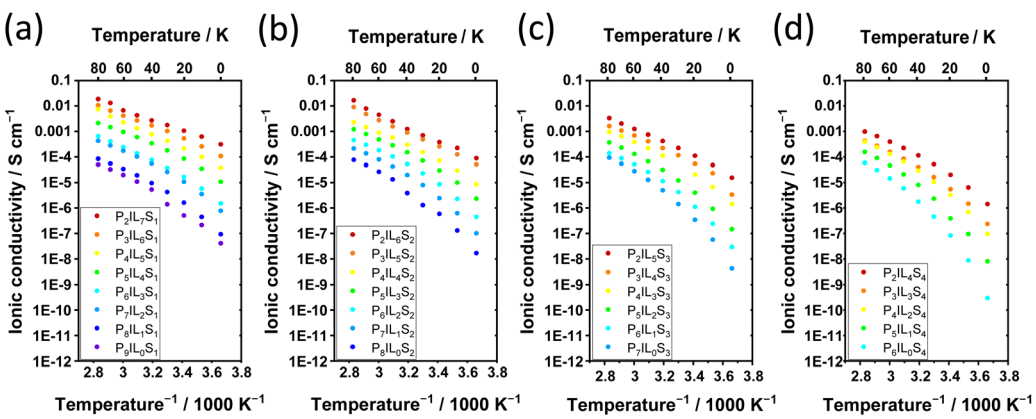


Fig. 4 Temperature dependent ionic conductivities of ternary electrolytes with PEODA, $Pyr_{14}TFSI$, and LiTFSI. Ionic conductivities plotted over inverse temperature and temperature; with LiTFSI compositions of (a) 10 wt%, (b) 20 wt%, (c) 30 wt%, and (d) 40 wt%.

$Pyr_{14}TFSI$ when increasing the temperature from 40 °C to 60 °C (Fig. 3a, d and e). When increasing the temperature even further to 70 °C and 80 °C, ionic conductivities of 10 mS $cm^{-1}$ and higher are reached, Fig. 3f and g.

In order to provide a high ionic conductivity for a broad variety of mass ratios, a temperature of 60 °C (Fig. 3a) is chosen for further analysis. The conductivity range at this temperature differs by several orders of magnitude. In order to understand this behavior, the ionic conductivity $\sigma$ of an electrolyte mixture can be viewed as a function of number density $n$, charge $q$ and mobility $\mu$ of ions, see eqn (1).[13]

$$\sigma = \sum n \cdot q \cdot \mu \quad \left| \begin{array}{l} \sigma = \text{ionic conductivity / mS cm}^{-1} \\ n = \text{number density of free charged species / m}^{-3} \\ q = \text{charge of ions / C} \\ \mu = \text{mobility of ions / m}^2\ \text{V}^{-1}\ \text{s}^{-1} \end{array} \right. \quad (1)$$

The highest conductivities are achieved with high $Pyr_{14}TFSI$ content. Samples with a $Pyr_{14}TFSI$ content of ≥50 wt% show conductivities greater than 1 mS $cm^{-1}$, while electrolyte samples with high PEODA as well as high LiTFSI content show comparatively low conductivities. $Pyr_{14}TFSI$ is very ion conductive because the liquid state of the molten salt results in a high mobility $\mu$ of charge carriers.[26] Exchanging PEODA by $Pyr_{14}TFSI$ elevates the number density $n$ and the overall amount of charges because the concentration of single charge ions like $Pyr_{14}^{+}$ and $TFSI^{-}$ is increased. In comparison to $Pyr_{14}TFSI$ and LiTFSI, PEODA is non-ionic and therefore decreases the number density of free charged species $n$ and the charge $q$ when increased. Furthermore, when PEODA is cross-linked, it turns from a liquid into a solid. This additionally decreases the ionic conductivity by reducing the overall mobility $\mu$. To achieve conductivities as high as possible, PEODA is therefore reduced in amount to a minimum of 20 wt%. Nonetheless, PEODA is necessary because it is the key component enabling a liquid state as well as the solvent-free phase transition from liquid to solid as described earlier. An increased LiTFSI content improves the ion conductivity only to some extent. While the interaction of ethylene oxide from PEODA and $Li^{+}$ promotes the LiTFSI dissociation and thereby the number density of free charged species $n$, the formation of ion clusters at high LiTFSI concentrations decreases the ionic conductivity.[27,28] Thus $[Li(TFSI)_n]^{(n-1)-}$-complexes are formed, leading to a lower mobility $\mu$.[29] These effects lead to an optimal low LiTFSI content of 10 wt%. With a PEODA content of 20 wt% the ionic conductivity is 6.8 mS $cm^{-1}$ for sample $P_2IL_7S_1$. When the LiTFSI content is increased, the ionic conductivity is decreased ($P_2IL_6S_2$: 4.5 mS $cm^{-1}$; $P_2IL_5S_3$: 1.3 mS $cm^{-1}$; $P_2IL_4S_4$: 0.4 mS $cm^{-1}$). In conclusion, low PEODA-, high $Pyr_{14}TFSI$- and moderate LiTFSI-contents are optimal for high ionic conductivity.

The ionic conductivity behavior over the inverse of temperature can give insights into the phase behavior as well as the temperature dependency of ion conduction in electrolytes (Fig. 4).[13]

In Fig. 4a, the plots at high polymer ratios of ≥40 wt% show a non-linear curved trend of the ionic conductivity (logarithmic scaling) over the inverse temperature, which represents typical VFT (Vogel–Fulcher–Tammann) behavior.[13] Therefore, the temperature dependent ionic conductivity is described by the VFT equation (eqn (2)). The VFT equation was originally postulated to describe the viscosity behavior of amorphous polymers above the glass transition temperature $T_G$. Because the viscosity and ion mobility can depend on each other, the VFT equation is widely used in polymer electrolyte research to describe the temperature dependency of the ionic conductivity.[30] The ion transport is described by the activation energy for ionic conduction $E_A$, the ideal glass transition temperature $T_0$ also known as Vogel temperature (usually about 50 K below $T_G$), the Boltzmann constant $k_B$ and the pre-exponential factor $\sigma_0$.

$$\sigma(T) = \sigma_0 \cdot \exp\left[\frac{-E_A}{k_B \cdot (T - T_0)}\right] \quad \left| \begin{array}{ll} \sigma = & \text{ionic conductivity / mS cm}^{-1} \\ \sigma_0 = & \text{pre-exponential factor / mS cm}^{-1} \\ E_A = & \text{activation energy for ionic conduction / eV} \\ k_B = & \text{Boltzmann constant / eV K}^{-1} \\ T = & \text{temperature / K} \\ T_0 = & \text{ideal glass transition temperature / K} \end{array} \right. \quad (2)$$

As shown from Fig. 4a–d, this behavior is valid for all compositions with a solid content (PEODA and LiTFSI) ≥50 wt%. The characteristic bending of the logarithmic scaled conductivity over the inverse temperature is caused by the reduction of the denominator $T$ by $T_0$ in the exponent of eqn (2). In Fig. 4d a steeper slope is seen from $P_2IL_4S_4$ to $P_6IL_0S_4$. This highlights an increased temperature influence when the liquid content ($Pyr_{14}TFSI$) is exchanged by PEODA. This is explained by the strong temperature dependency of the segmental motions in polymers, which facilitate ion conduction.[15] Due to the VFT behavior, an amorphous state without phase transitions is assumed in the measured temperature range. This is verified by DSC *e.g.*, for $P_2IL_5S_3$ (see ESI, Fig. 14†).

With increasing $Pyr_{14}TFSI$ and decreasing PEODA amounts, a transition from a VFT (sample $P_9IL_0S_1$) to a linear behavior (sample $P_2IL_7S_1$) occurs for LiTFSI shares of ≤30 wt% (Fig. 4a–c). The linearity of the logarithmically scaled ionic conductivity over the inverse temperature is observed when $T_0 \ll T$. The ionic conductivities of these electrolytes follow the Arrhenius equation in which $T_0$ is not considered, see eqn (3).

$$\sigma(T) = \sigma_0 \cdot \exp\left[\frac{-E_A}{k_B \cdot T}\right] \quad (3)$$

$\sigma$ = ionic conductivity / mS cm$^{-1}$
$\sigma_0$ = pre-exponential factor / mS cm$^{-1}$
$E_A$ = activation energy for ionic conduction / eV
$k_B$ = Boltzmann constant / eV K$^{-1}$
$T$ = temperature / K

This behavior is typical for high Li salt or high ionic liquid content polymer electrolytes called PISE (polymer-in-salt electrolyte) or iongels.[13,31,32] For $P_2IL_7S_1$ (Fig. 4a, red) and $P_2IL_5S_3$ (Fig. 4c, red) the activation energy $E_A$ was derived by fitting the values according to the Arrhenius equation (see ESI, Fig. 15†). Two major differences are visible when comparing the Ionic conductivities plotted over inverse temperature for $P_2IL_7S_1$ and $P_2IL_5S_3$. First the values for $P_2IL_7S_1$ show higher conductivities as a result of the higher ion mobility $\mu$ discussed previously, which is expressed by a higher $\sigma_0$ in the Arrhenius equation. Second the slope of the ionic conductivities plotted over inverse temperature is lower for $P_2IL_7S_1$ compared to $P_2IL_5S_3$, which is expressed by a lower $E_A$ in the Arrhenius equation. The activation energies are 0.18 eV and 0.23 eV for $P_2IL_7S_1$ and $P_2IL_5S_3$, respectively. The values are in agreement with comparable electrolytes from literature.[33]

In summary, an Arrhenius type conductivity with low temperature dependency is achieved for electrolytes with high $Pyr_{14}TFSI$ portion. This behavior is favorable compared to VFT-like properties, in which the conductivity drops faster with decreasing temperature. Therefore, Li metal batteries containing electrolytes with high $Pyr_{14}TFSI$ content can be run in a wider temperature range.

### Safety and stability

Apart from high ionic conductivity, electrolytes have to match the safety expectations for Li metal batteries. Especially the formation of HSAL, for example Li dendrite growth through the separator/electrolyte, cause a conductive connection of the electrodes and lead to a cell failure by short-circuit. To investigate the ability of the electrolytes of preventing short-circuits by dendrites single discharge polarization tests are performed, see Fig. 5. A rapid voltage drop indicates a short-circuit. For a symmetric Li||Li cell with $P_2IL_7S_1$, a short-circuit occurs after 0.42 mA h cm$^{-2}$, which is too low to be used in practice. But for the Li||Li cell using an electrolyte with increased LiTFSI content like $P_2IL_5S_3$ a short-circuit occurs after deposition of 8.80 mA h cm$^{-2}$. The capacity is increased by a factor of 20 making it applicable in practice. By partially exchanging $Pyr_{14}$-TFSI with LiTFSI, a trade off is made. On the one hand, an increased solid content (LiTFSI or PEODA) reduces the ionic conductivity as discussed above. On the other hand, a reduced liquid content ($Pyr_{14}TFSI$) improves the mechanical stability of the electrolyte into a more rigid electrolyte, which reduce the risk of short-circuits caused by dendrites.[34] The reason for increasing the solid content by LiTFSI instead by PEODA is discussed in the ESI (Fig. 16†).

The oxidative stability of the electrolyte $P_2IL_5S_3$ is studied by linear sweep voltammetry with a sweep rate of 0.5 mV s$^{-1}$ (OCV to 6 V) in a SST||Li setup (Fig. 5b). A major current increase is observed for voltages >5.0 V. The current exceeds a value of 10 μA at 5.03 V and increases rapidly from >5.5 V. Therefore accoding to LSV the electrolyte is suitable to operate within the voltage range of common cathode materials like LFP with a average charge–discharge voltage of 3.4 V – 3.8 V *vs.* Li|Li$^+$.[25,35,36] Nonetheless, as shown by Jung *et al.* the applicability of an electrolyte towards a cathode material is not only determined by the high voltage stability of an electrolyte, but also by the chemistry of the cathode materials.[37,38] As mentioned in their work additionally to the electrochemical oxidation pathway of the electrolyte, also the chemical oxidation has to be considered. Due to oxygen release of the NMC622 cathode material at high rates of discharge, which is excellerated at increased temperatures, the overall stability of the system can be limited to voltages <5 V *vs.* Li|Li$^+$. Furthermore, as reviewed by Cabañero *et al.* the high voltage stability of the electrolyte is effected by the chemical reactivity of the cathode aswell as its surface area.[39] In case of TSPEs the oxidation of PEO or PEODA at the cathode interface can limit the electrolyte stability and the application towards NMC622.[35,40,41] Therefore, additionally to the LSV measurement, the effect of cycling towards LFP and NMC622 are shown in Fig. 10 and 19 in the ESI.† In order to apply NMC cathodes the TSPE composition has to be modified, which is of interest in an upcoming work.

The temperature stability of the electrolyte is measured by TGA over a temperature range from 20 °C to 600 °C. At ≥300 °C the decomposition of PEODA is observed.[42] From 360 °C on, LiTFSI and $Pyr_{14}TFSI$ decompose.[42–44] In summary, an overall high temperature stability of 300 °C is reached, which is

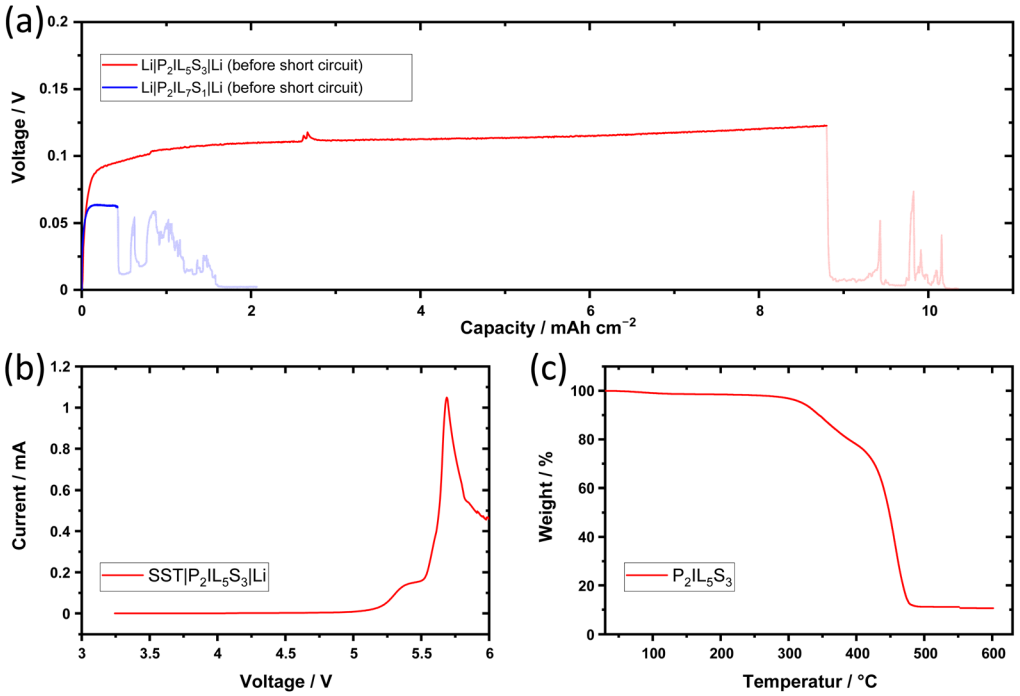


Fig. 5 Safety & thermal stability of ternary solid electrolyte. (a) Li|$P_2IL_5S_3$|Li cell - single discharge polarization of 0.1 mA $cm^{-2}$ until failure at 60 °C; (b) LSV of a SST|$P_2IL_5S_3$|Li cell from OCV to 6 V with a scan rate of 0.5 mV $s^{-1}$ at 60 °C; (c) TGA of $P_2IL_5S_3$ from 20 °C to 600 °C.

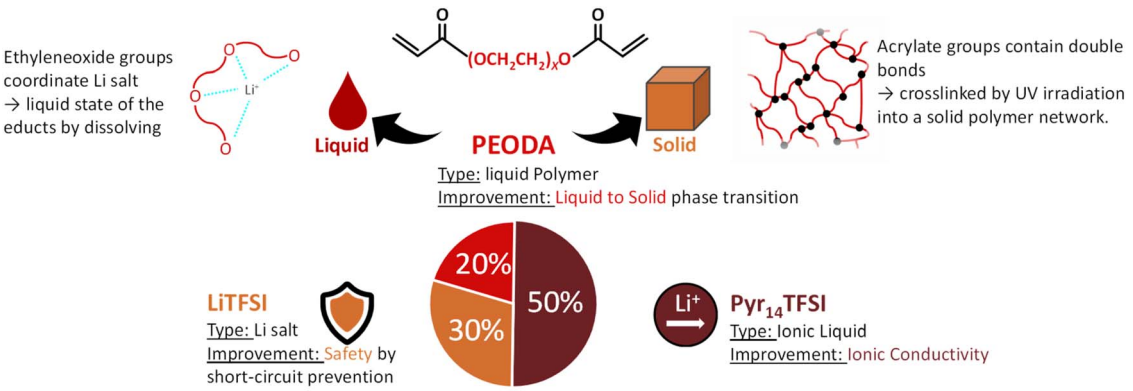


Fig. 6 Summary of the main improvements provided by the ingredients of the $P_2IL_5S_3$ electrolyte.

comparable to PEO-$Pyr_{14}$TFSI-LiTFSI-based electrolytes reported in literature.[44]

The optimized TSPE composition of $P_2IL_5S_3$ is shown in Fig. 6. In summary, the 20 wt% of PEODA enable the liquid to solid phase transition, the 50 wt% of $Pyr_{14}$TFSI boost the ionic conductivity compared to IL-free TSPEs and the 30 wt% LiTFSI improve the short-circuit prevention.

## Electrochemical performance

To reveal electrochemical performance and limitations of the electrolyte, the transference number $t_+$ is measured by the Bruce–Vincent method.[45] A small constant voltage ($\Delta V$) of 20 mV ± 1 mV is applied to a Li|$P_2IL_5L_3$|Li cell. The current drops from the initial current ($I_0$) until a constant concentration gradient of ions over the electrolyte is achieved and a lower steady state current ($I_{SS}$) is reached. In the ideal case, the steady state current $I_{SS}$ is divided by the initial current $I_0$ results in the $t_+$, see eqn (4).

$$t_+ = \frac{I_{ss}}{I_0} \quad \begin{array}{l} t_+ = \text{transference number} \\ I_0 = \text{initial current / A} \\ I_{ss} = \text{steady state current / A} \end{array} \tag{4}$$

For solid electrolytes, overvoltages resulting from the interfacial/interphasial (I&I) resistance must be considered, as well. The extended equation with correction terms for the I&I resistance with the I&I resistance before polarization $R_0$ and the I&I resistance under steady state $R_{SS}$ is shown in eqn (5).

$$t_+ = \frac{I_{ss}(\Delta V - I_0 R_0)}{I_0(\Delta V - I_{ss} R_{ss})} \quad (5)$$

$t_+$ = transference number
$\Delta V$ = applied potential / V
$I_0$ = initial current / A
$I_{ss}$ = steady-state current / A
$R_0$ = interfacial and interphasial resistance before polarization / Ω
$R_{ss}$ = interfacial and interphasial resistance at steady state / Ω

I&I resistances are determined by electrochemical impedance spectroscopy. The impedance spectra are fitted by a representative circuit built of the elements: resistor, capacitor and transport (Warburg) element. The simplified Randles Circuit represents an ideal symmetric cell without diffusion and is extended to use it for fitting the Nyquist plots, see inset Fig. 8a. $R_1$ is the electrolyte resistance. The parallel connection of the $R_2/C_2$ element represents the Li|electrolyte interface. $C_2$ is the capacitive behavior of the ionic double layer at the Li|electrolyte interface and $R_2$ represents the resistance for charge-transfer at the Li|electrolyte interface. A transport (Warburg) element ($W_1$) for semi-infinite diffusion is used representing Li-ion diffusion at low frequencies. Because the $R_1 + (R_2/C_2) + W_1$ circuit does not take into account non-ideal phenomenons like the formation of an additional interphase by a SEI a second $R_3/C_3$ element is added.[46] The equivalent circuit $R_1 + (R_2/C_2) + (R_3/C_3) + W_1$ is shown in Fig. 7.

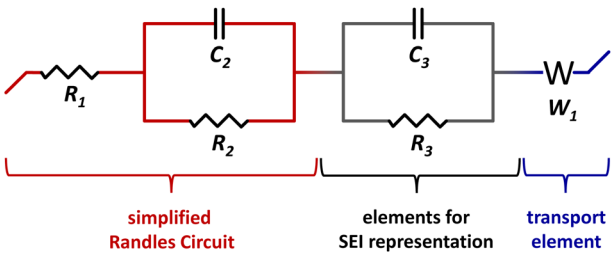


Fig. 7 Equivalent circuit used to fit impedance plots.

The current response of a Li| $P_2IL_5L_3$|Li cell at a constant voltage of 19.2 mV is shown in Fig. 8a ($I_0$ = 0.2493 mA, $I_{SS}$ = 0.0254 mA). To determine the $t_+$ by the Bruce–Vincent method, impedance spectra are measured before and after polarization. The inset shows the Nyquist plots before and after polarization fitted by the equivalent circuit of Fig. 7 ($R_0$ = 28.97 Ω, $R_{SS}$ = 29.25 Ω). An average $t_+$ of 0.063 ± 0.004 is determined. The $t_+$ highlights the formation of $[Li(TFSI)_n]^{(n-1)-}$ complexes at high LiTFSI content, which, on one hand, decreases Li-ion mobility and reduces $t_+$, but on the other hand, results in a great prevention of dendrite growth, as discussed before. The value is comparable to other $Pyr_{14}$TFSI-based systems form literature with a $t_+$ of 0.09.[47]

A charge-pulse method was applied to investigate the limiting current density.[48] The resulting voltage over time plots for charge-pulses of 1.2 mA cm$^{-2}$ to 2.2 mA cm$^{-2}$ are shown in Fig. 8b. The cutoff voltage (1 V) is reached faster with increasing current density, indicating a faster depletion of $Li^+$ in the electrolyte at the Li metal|electrolyte interface. As described by Wetjen *et al.*, the depletion time and the current density are used to derive the inverse charge density over

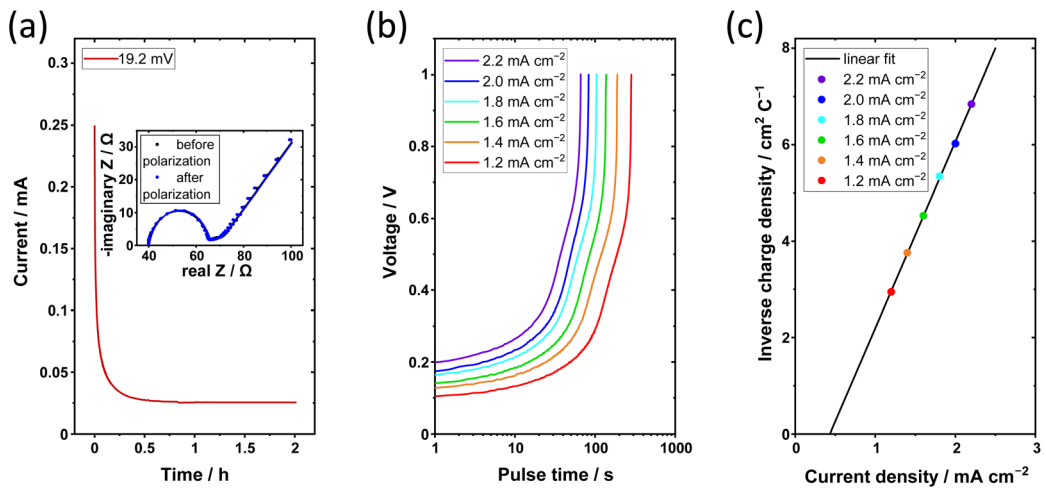


Fig. 8 Electrochemical limitations of the ternary solid electrolyte. (a) Constant voltage polarization at 19.2 mV of a Li|$P_2IL_5L_3$|Li cell at 60 °C, inset shows impedance measurement before and after polarization; (b) charge pulses from 1.2 mA cm$^{-2}$ to 2.2 mA cm$^{-2}$ of a Li|$P_2IL_5L_3$|Li cell at 60 °C; (c) inverse charge density over current density, intersection of the linear fit with the current density axis represents the limiting current density.

current density, see Fig. 8c. By linear fitting the limiting current density is obtained from the $x$-axis intercept. The resulting limiting current density is $0.46 \pm 0.03$ mA cm$^{-2}$. This high limiting current density highlights that despite the low $t_+$ an electrolyte capable of cycling at sufficient rates has been synthesized.

### Reversibility of Li metal electrodeposition and -dissolution

The Coulombic efficiency of Li metal electrodeposition and -dissolution is studied by cycling a Cu||Li cell.[49] During electrodeposition/dissolution of Li metal on/from the Cu surface, active Li is lost by the formation of dead Li or side reactions causing a Coulombic efficiency <100% such as SEI formation. In a Cu||Li cell with the electrolyte $P_2IL_5S_3$, a Coulombic efficiency of 58% is determined in the first cycle (Fig. 9a). With increasing cycle number, the Coulombic efficiency increases to 93% where it stabilizes after the 90$^{th}$ cycle. In comparison to PEO$_{ref}$ from literature the Coulombic efficiency of $P_2IL_5L_3$ in Cu||Li cells is higher as well as more stable.[22] The homogeneity of Li metal deposition is further evaluated by using a laser scanning microscope, see Fig. 18.†

The stability of Li cycling is studied in a Li||Li cell. The voltage over time profile is shown in Fig. 9b. The high overvoltage in the first cycle (−0.14 V, 0.12 V) is reported to be caused by the native SEI of $Li_2O$ and $Li_2CO_3$ on the Li metal surface.[50] After the first three cycles, the overvoltage drops to ±0.09 V due to the deposition of fresh Li metal without a thick SEI layer, as well as an presumably increased Li surface area.[8] Because of the accumulation of dead Li, the Li-ion diffusion through the I&I of the Li metal anode becomes more resistive at later cycles leading to the overvoltage slightly increasing to ±0.12 V after 500 h.[51]

Additionally, the stability of Li cycling as well as the Coulombic efficiency of Li metal electrodeposition and -dissolution is verified in LFP||Li cells with $P_2IL_5S_3$ electrolyte, see Fig. 10. Due to flexibility of the electrolyte the rough cathode surface is contacted well by the $P_2IL_5L_3$ electrolyte, see Fig. 17 in the ESI.† The Coulombic efficiency of LFP|P2IL5S3|Li cells is 99% in the first cycle and drops to an average of 94% after 10 cycles at which it remains stable, see Fig. 10a. The Coulombic efficiency is slightly higher than in Cu||Li cells (93%) which is possibly caused by a higher Li loss of highly reactive HSAL on the Cu surface. During cycling, the specific capacity remains at

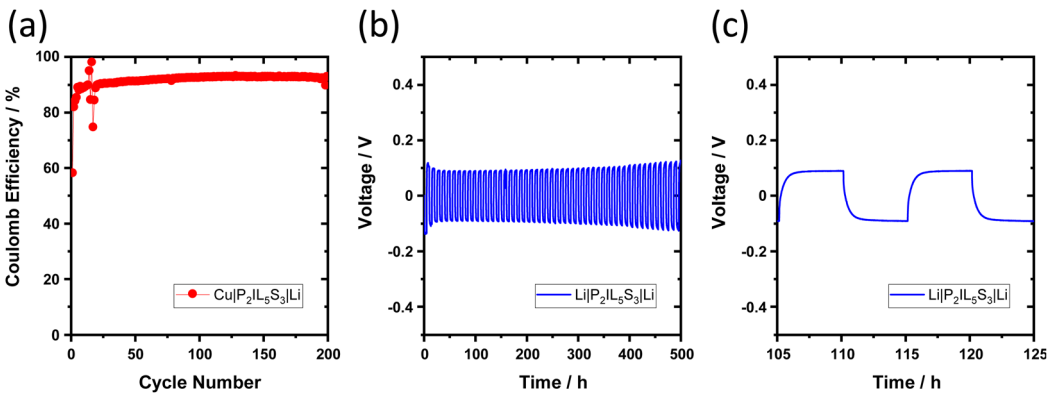


Fig. 9 Li metal electrodeposition and -dissolution with a ternary solid electrolyte. Galvanostatic cycling of (a) Cu|$P_2IL_5L_3$|Li cell at 0.1 mA h cm$^{-2}$ for 0.1 mA cm$^{-2}$ per step at 60 °C; (b) Li|$P_2IL_5L_3$|Li cell at 0.1 mA cm$^{-2}$ for 0.5 mA h cm$^{-2}$ per step at 60 °C; (c) voltage profile of b from 105 h to 125 h.

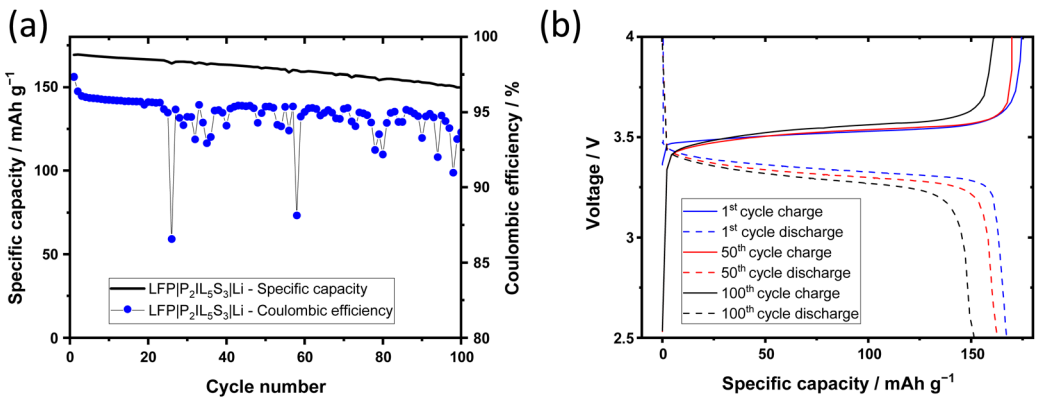


Fig. 10 Li metal electrodeposition and −dissolution with a ternary solid electrolyte in LFP|$P_2IL_5S_3$|Li cells at 0.05 mA cm$^{-2}$ for 100 cycles at 60 °C. (a) Specific capacity and Coulombic efficiency over cycle number; (b) voltage evolution of the 1$^{st}$, 50$^{th}$, and 100$^{th}$ cycle over the specific capacity.

Table 2 Comparison of the developed $P_2IL_5S_3$ to $PEO_{ref}$ from literature

| Name | Polymer type | Composition[a] | Capacity utilization | Processing without temperature or solvents | Elastic modulus |
|---|---|---|---|---|---|
| $P_2IL_5S_3$ | Liquid PEODA ($M_n$: 700) | 20 wt% PEODA<br>50 wt% IL<br>30 wt% Li salt | 8.8 mA h $cm^{-2}$ | Yes | 3.2 MPa |
| $PEO_{ref}$ | Solid PEO ($M_n$: 4 mio) | 28 wt% PEO<br>54 wt% IL<br>18 wt% Li salt | 1.6 mA h $cm^{-2}$ | No | 0.3 MPa |

[a] Without BP.



a high level, it starts at 169 mA h $g^{-1}$ which is close to the maximum theoretical capacity of LFP. At the 100$^{th}$, cycle 88% (150 mA h $g^{-1}$) of the initial capacity is maintained, see Fig. 10a and b. During cycling, the overvoltage increases slightly which can be explained by the SEI and dead lithium formation discussed previously.

Finally, the $P_2IL_5S_3$ is compared to a PEO-based electrolyte $PEO_{ref}$ from literature, see Table 2.[20,22] As shown in this work by using PEODA instead of PEO the electrolyte can be processed without elevated temperature or the application of processing solvents. Furthermore, the higher Li salt content of $P_2IL_5S_3$ (30%) compared to $PEO_{ref}$ (18%) enables a higher capacity utilization (short-circuit prevention). Due to the smaller polymer chains $P_2IL_5S_3$ (3.2 MPa) is more rigid compared to $PEO_{ref}$ (0.3 MPa) providing a more stable film during application.

## Conclusion

In this study, a ternary electrolyte (containing polymer, ionic liquid and Li salt) was studied. An alternative electrolyte processing without processing solvents or hot pressing, but taking advantage from a liquid to solid phase transition was enabled. The electrolyte system was sequentially optimized in relation to ionic conductivity and safety. The resulting electrolyte has a high ionic conductivity of >1 mS $cm^{-1}$ at 60 °C and is able to prevent short-circuits due to dendrite growth when containing high salt contents. The electrolyte has a sufficient limiting current density of 0.46 mA $cm^{-2}$ as well as a high thermal stability of >300 °C.

The unique processing at RT and without processing solvents presented in this work paves the way for a new research direction towards ternary electrolytes. Different from gel or solvated processing, the liquid electrolyte can directly be coated and solidified on electrodes allowing for an improved contact towards the electrode surface, thin film applications and fast processing. Also, different coatings for anode and cathode, that allow for electrolyte compositions matching the requirements, could be applied.

## Author contributions

Lukas Herbers[A] performed the synthesis of electrolytes, cell assembly, electrochemical measurements and evaluation of data. The DSC and TGA measurements were performed by Debbie Berghus[A]. The KF measurements were performed by Lea-Sophie Kemper[A]. Martin Winter[A,B] and Peter Bieker[B] created the concept of work and supervised the work. Lukas Herbers[A] wrote the manuscript through contributions of Verena Küpers[A], Peter Bieker[B] and Martin Winter[A,B].

## Conflicts of interest

There are no conflicts to declare.

## Acknowledgements

The authors thank the Ministry for Culture and Science of North Rhine Westphalia (Germany) for funding this work within the International Graduate School for Battery Chemistry, Characterization, Analysis, Recycling and Application (BACCARA).

## References

1 Z. Cheng, T. Liu, B. Zhao, F. Shen, H. Jin and X. Han, Recent advances in organic–inorganic composite solid electrolytes for all-solid-state lithium batteries, *Energy Storage Mater*, 2021, **34**, 388–416.
2 Daniel, C. and Besenhard, J. O., *Handbook of battery materials, 2., completely revised and enlarged edition, reprinted*, Wiley-VCH, Weinheim, 2012.
3 M. Winter, B. Barnett and K. Xu, Before Li Ion Batteries, *Chem. Rev.*, 2018, **118**, 11433–11456.
4 J. Janek and W. G. Zeier, A solid future for battery development, *Nat. Energy*, 2016, **1**, 16141.
5 Z. Jiang, Q. Han, S. Wang and H. Wang, Reducing the Interfacial Resistance in All-Solid-State Lithium Batteries Based on Oxide Ceramic Electrolytes, *ChemElectroChem*, 2019, **6**, 2970–2983.
6 X. Wang, W. Mai, X. Guan, Q. Liu, W. Tu, W. Li, F. Kang and B. Li, Recent Advances of Electroplating Additives Enabling Lithium Metal Anodes to Applicable Battery Techniques, *Energy Environ. Mater.*, 2021, **4**, 284–292.
7 B. S. Vishnugopi, A. Verma and P. P. Mukherjee, Morphology-Safety Implications of Interfacial Evolution in Lithium Metal Anodes, *J. Phys. Chem. C*, 2020, **124**, 16784–16795.
8 G. Bieker, M. Winter and P. Bieker, Electrochemical *in situ* investigations of SEI and dendrite formation on the

lithium metal anode, *Phys. Chem. Chem. Phys.*, 2015, **17**, 8670–8679.

9 A. Manthiram, X. Yu and S. Wang, Lithium battery chemistries enabled by solid-state electrolytes, *Nat. Rev. Mater.*, 2017, **2**, 16103.

10 W. Zhao, J. Yi, P. He and H. Zhou, Solid-State Electrolytes for Lithium-Ion Batteries: Fundamentals, Challenges and Perspectives, *Electrochem. Energy Rev.*, 2019, **2**, 574–605.

11 D.-H. Liu, Z. Bai, M. Li, A. Yu, D. Luo, W. Liu, L. Yang, J. Lu, K. Amine and Z. Chen, Developing high safety Li-metal anodes for future high-energy Li-metal batteries: strategies and perspectives, *Chem. Soc. Rev.*, 2020, **49**, 5407–5445.

12 J. Wu, L. Yuan, W. Zhang, Z. Li, X. Xie and Y. Huang, Reducing the thickness of solid-state electrolyte membranes for high-energy lithium batteries, *Energy Environ. Sci.*, 2021, **14**, 12–36.

13 J. Mindemark, M. J. Lacey, T. Bowden and D. Brandell, Beyond PEO—Alternative host materials for Li + -conducting solid polymer electrolytes, *Prog. Polym. Sci.*, 2018, **81**, 114–143.

14 Q. Yu, K. Jiang, C. Yu, X. Chen, C. Zhang, Y. Yao, B. Jiang and H. Long, Recent progress of composite solid polymer electrolytes for all-solid-state lithium metal batteries, *Chin. Chem. Lett.*, 2021, **32**, 2659–2678.

15 L. Li, H. Duan, J. Li, L. Zhang, Y. Deng and G. Chen, Toward High Performance All-Solid-State Lithium Batteries with High-Voltage Cathode Materials: Design Strategies for Solid Electrolytes, Cathode Interfaces, and Composite Electrodes, *Adv. Energy Mater.*, 2021, **11**, 2003154.

16 Z. Wu, Z. Xie, A. Yoshida, Z. Wang, X. Hao, A. Abudula and G. Guan, Utmost limits of various solid electrolytes in all-solid-state lithium batteries: A critical review, *Renewable Sustainable Energy Rev.*, 2019, **109**, 367–385.

17 S. Qian, H. Chen, Z. Wu, D. Li, X. Liu, Y. Tang and S. Zhang, Designing Ceramic/Polymer Composite as Highly Ionic Conductive Solid-State Electrolytes, *Batteries Supercaps*, 2021, **4**, 39–59.

18 J. R. Nair, L. Imholt, G. Brunklaus and M. Winter, Lithium Metal Polymer Electrolyte Batteries: Opportunities and Challenges, *Electrochem. Soc. Interface*, 2019, **28**, 55–61.

19 J. Li, F. Li, L. Zhang, H. Zhang, U. Lassi and X. Ji, Recent applications of ionic liquids in quasi-solid-state lithium metal batteries, *Green Chemical Engineering*, 2021, **2**, 253–265.

20 G. T. Kim, G. B. Appetecchi, M. Carewska, M. Joost, A. Balducci, M. Winter and S. Passerini, UV cross-linked, lithium-conducting ternary polymer electrolytes containing ionic liquids, *J. Power Sources*, 2010, **195**, 6130–6137.

21 L. M. McGrath and J. F. Rohan, Pyrrolidinium Containing Ionic Liquid Electrolytes for Li-Based Batteries, *Molecules*, 2020, **25**, 6002.

22 M. Zhang, A. L. Gui, W. Sun, J. Becking, O. Riedel, X. He, D. Berghus, V. Siozios, D. Zhou, T. Placke, *et al.*, High Capacity Utilization of Li Metal Anodes by Application of Celgard Separator-Reinforced Ternary Polymer Electrolyte, *J. Electrochem. Soc.*, 2019, **166**, A2142–A2150.

23 J. Henschel, J. M. Dressler, M. Winter and S. Nowak, Reaction Product Analyses of the Most Active "Inactive" Material in Lithium-Ion Batteries—The Electrolyte. I: Themal Stress and Marker Molecules, *Chem. Mater.*, 2019, **31**, 9970–9976.

24 X. Zeng, L. Dong, J. Fu, L. Chen, J. Zhou, P. Zong, G. Liu and L. Shi, Enhanced interfacial stability with a novel boron-centered crosslinked hybrid polymer gel electrolytes for lithium metal batteries, *Chem. Eng. J.*, 2022, **428**, 131100.

25 A. Ahniyaz, I. de Meatza, A. Kvasha, O. Garcia-Calvo, I. Ahmed, M. F. Sgroi, M. Giuliano, M. Dotoli, M.-A. Dumitrescu, M. Jahn, *et al.*, Progress in solid-state high voltage lithium-ion battery electrolytes, *Adv. Appl. Energy*, 2021, **4**, 100070.

26 A. K. Tripathi, Ionic liquid–based solid electrolytes (ionogels) for application in rechargeable lithium battery, *Mater. Today Energy*, 2021, **20**, 100643.

27 P. M. Bayley, G. H. Lane, L. J. Lyons, D. R. MacFarlane and M. Forsyth, Undoing Lithium Ion Association in Ionic Liquids through the Complexation by Oligoethers, *J. Phys. Chem. C*, 2010, **114**, 20569–20576.

28 T. Umecky, Y. Saito, Y. Okumura, S. Maeda and T. Sakai, Ionization condition of lithium ionic liquid electrolytes under the solvation effect of liquid and solid solvents, *J. Phys. Chem. B*, 2008, **112**, 3357–3364.

29 S. Kim, M. Lee, C. Park, A. Park, S. Kwon, J. Cho, S. Kim, S. Rho and W. B. Lee, Molecular dynamics study on lithium-ion transport in PEO branched nanopores with $PYR_{14}$TFSI ionic liquid, *Battery Energy*, 2022, **1**, 20210013.

30 K. M. Diederichsen, H. G. Buss and B. D. McCloskey, The Compensation Effect in the Vogel–Tammann–Fulcher (VTF) Equation for Polymer-Based Electrolytes, *Macromolecules*, 2017, **50**, 3831–3840.

31 D. Aidoud, D. Guy-Bouyssou, D. Guyomard, J. Le Bideau and B. Lestriez, Photo-Polymerized Organic Host Network of Ionogels for Lithium Batteries: Effects of Mesh Size and of Ethylene Oxide Content, *ECS Trans.*, 2018, **86**, 163–178.

32 L. Chen and L.-Z. Fan, Dendrite-free Li metal deposition in all-solid-state lithium sulfur batteries with polymer-in-salt polysiloxane electrolyte, *Energy Storage Mater*, 2018, **15**, 37–45.

33 M. Montanino, M. Moreno, F. Alessandrini, G. B. Appetecchi, S. Passerini, Q. Zhou and W. A. Henderson, Physical and electrochemical properties of binary ionic liquid mixtures: $(1-x)$ $PYR_{14}$TFSI–$(x)$ $PYR_{14}IM_{14}$, *Electrochim. Acta*, 2012, **60**, 163–169.

34 C. Zhu, Y. Ning, Y. Jiang, G. Li and Q. Pan, Double-Network Polymer Electrolytes with Ionic Liquids for Lithium Metal Batteries, *Polymers*, 2022, **14**.

35 X. Yang, M. Jiang, X. Gao, D. Bao, Q. Sun, N. Holmes, H. Duan, S. Mukherjee, K. Adair, C. Zhao, *et al.*, Determining the limiting factor of the electrochemical stability window for PEO-based solid polymer electrolytes: main chain or terminal –OH group?, *Energy Environ. Sci.*, 2020, **13**, 1318–1325.

36 Y. Zheng, N. Xu, S. Chen, Y. Liao, G. Zhong, Z. Zhang and Y. Yang, Construction of a Stable $LiNi_{0.8}Co_{0.1}Mn_{0.1}O_2$

(NCM811) Cathode Interface by a Multifunctional Organosilicon Electrolyte Additive, *ACS Appl. Energy Mater.*, 2020, **3**, 2837–2845.

37 R. Jung, P. Strobl, F. Maglia, C. Stinner and H. A. Gasteiger, Temperature Dependence of Oxygen Release from $LiNi_{0.6}Mn_{0.2}Co_{0.2}O_2$ (NMC622) Cathode Materials for Li-Ion Batteries, *J. Electrochem. Soc.*, 2018, **165**, A2869–A2879.

38 R. Jung, M. Metzger, F. Maglia, C. Stinner and H. A. Gasteiger, Oxygen Release and Its Effect on the Cycling Stability of $LiNi_xMn_yCo_zO_2$ (NMC) Cathode Materials for Li-Ion Batteries, *J. Electrochem. Soc.*, 2017, **164**, A1361–A1377.

39 M. A. Cabañero Martínez, N. Boaretto, A. J. Naylor, F. Alcaide, G. D. Salian, F. Palombarini, E. Ayerbe, M. Borras and M. Casas-Cabanas, Are Polymer-Based Electrolytes Ready for High-Voltage Lithium Battery Applications? An Overview of Degradation Mechanisms and Battery Performance, *Adv. Energy Mater.*, 2022, **12**, 2201264.

40 K. Nie, X. Wang, J. Qiu, Y. Wang, Q. Yang, J. Xu, X. Yu, H. Li, X. Huang and L. Chen, Increasing Poly(ethylene oxide) Stability to 4.5 V by Surface Coating of the Cathode, *ACS Energy Lett.*, 2020, **5**, 826–832.

41 Y.-C. Jung, M.-S. Park, D.-H. Kim, M. Ue, A. Eftekhari and D.-W. Kim, Room-Temperature Performance of Poly(Ethylene Ether Carbonate)-Based Solid Polymer Electrolytes for All-Solid-State Lithium Batteries, *Sci. Rep.*, 2017, **7**, 17482.

42 S. Li, Y.-M. Chen, W. Liang, Y. Shao, K. Liu, Z. Nikolov and Y. Zhu, A Superionic Conductive, Electrochemically Stable Dual-Salt Polymer Electrolyte, *Joule*, 2018, **2**, 1838–1856.

43 M. Nádherná, J. Reiter, J. Moškon and R. Dominko, Lithium bis(fluorosulfonyl)imide–$PYR_{14}$TFSI ionic liquid electrolyte compatible with graphite, *J. Power Sources*, 2011, **196**, 7700–7706.

44 M. Joost, G. T. Kim, M. Winter and S. Passerini, Phase stability of Li-ion conductive, ternary solid polymer electrolytes, *Electrochim. Acta*, 2013, **113**, 181–185.

45 J. Evans, C. A. Vincent and P. G. Bruce, Electrochemical measurement of transference numbers in polymer electrolytes, *Polymer*, 1987, **28**, 2324–2328.

46 A. Barai, K. Uddin, M. Dubarry, L. Somerville, A. McGordon, P. Jennings and I. Bloom, A comparison of methodologies for the non-invasive characterisation of commercial Li-ion cells, *Prog. Energy Combust. Sci.*, 2019, **72**, 1–31.

47 P. R. Chinnam, V. Chatare, S. Chereddy, R. Mantravadi, M. Gau, J. Schwab and S. L. Wunder, Multi-ionic lithium salts increase lithium ion transference numbers in ionic liquid gel separators, *J. Mater. Chem. A*, 2016, **4**, 14380–14391.

48 M. Wetjen, G.-T. Kim, M. Joost, M. Winter and S. Passerini, Temperature dependence of electrochemical properties of cross-linked poly(ethylene oxide)-lithium bis(trifluoromethanesulfonyl)imide-*N*-butyl-*N*-methylpyrrolidinium bis(trifluoromethanesulfonyl)imide solid polymer electrolytes for lithium batteries, *Electrochim. Acta*, 2013, **87**, 779–787.

49 B. D. Adams, J. Zheng, X. Ren, W. Xu and J.-G. Zhang, Accurate Determination of Coulombic Efficiency for Lithium Metal Anodes and Lithium Metal Batteries, *Adv. Energy Mater.*, 2018, **8**, 1702097.

50 J. Wellmann, J.-P. Brinkmann, B. Wankmiller, K. Neuhaus, U. Rodehorst, M. R. Hansen, M. Winter and E. Paillard, Effective Solid Electrolyte Interphase Formation on Lithium Metal Anodes by Mechanochemical Modification, *ACS Appl. Mater. Interfaces*, 2021, **13**, 34227–34237.

51 K.-H. Chen, K. N. Wood, E. Kazyak, W. S. LePage, A. L. Davis, A. J. Sanchez and N. P. Dasgupta, Dead lithium: mass transport effects on voltage, capacity, and failure of lithium metal anodes, *J. Mater. Chem. A*, 2017, **5**, 11671–11681.